

PWM Switched Capacitor-Based Cell-Level Power Balancing Converter Utilizing Diffusion Capacitance of Photovoltaic Cells

Masatoshi Uno, *Member, IEEE*, Yota Saito, Shinichi Urabe, and Masaya Yamamoto

Abstract— This paper proposes a novel PWM cell-level diffusion charge redistribution (DCR) converter based on a switched capacitor converter (SCC) utilizing diffusion capacitance of photovoltaic (PV) cells for PV modules under partial shading. Although a discrete inductor and capacitor are additionally necessary, Joule losses associated with switching operations can be reduced compared to the conventional capacitorless DCR converter. Firstly, ac impedance measurement for a PV cell with 125×125 mm was performed, and the diffusion capacitance values were measured to be approximately 6.0 mF at its maximum power point voltage of 0.574 V. Secondly, the theoretical loss model was derived based on the detailed analysis, and it revealed that an optimal duty cycle achieving the lowest Joule loss was dependent on shading conditions. Thirdly, a dual MPPT algorithm that controls duty cycles of not only the DCR converter but also a front-end boost converter is also proposed. With the dual MPPT control, the DPP converter operates at its optimal duty cycle to minimize the Joule loss while the boost converter seeks the MPP. The experimental results demonstrated that the maximum power significantly increased thanks to the DCR converter, and that both the DCR and boost converters operated with respective optimal duty cycles.

Keywords—Diffusion capacitance, photovoltaic cell, partial shading, switched capacitor converter (SCC), maximum power point tracking (MPPT).

I. INTRODUCTION

Partial shading on a photovoltaic (PV) panel comprising multiple substrings connected in series is known to cause serious issues, such as significant decrease in energy yield and occurrence of multiple maximum power points (MPPs). For instance, 10% equivalent area of partial shading on a PV module reportedly results in 30% reduction in power generation of the module as a whole [1]. Similar phenomena occur in curved PV panels, such as solar roofs for plug-in hybrid electric vehicles (PHEVs), due to uneven irradiance on the panel at all times, as depicted in Fig. 1. The impact of the reduced energy yield will be of serious concern in mobile and vehicular applications where space for PV panels is very limited.

Module-integrated converters (or dc optimizers) and micro-inverters that can mitigate the negative issues of partial shading have been extensively developed and commercialized [2], [3]. By applying these converters and inverters to substring level, all substrings in a panel can operate at each optimal point, contributing to increased energy yield even under partial shading conditions. However, since these converters and inverters must process the full power of panels/substrings, the cost and volume are prone to soar as numerous active and passive devices with relatively high-power rating are necessary.

The aforementioned module-integrated converters and micro-inverters are essentially a full power processing (FPP) converter that must be rated for the full power of panels/substrings. In contrast, differential power processing (DPP) converters literally process only differential power, hence allowing a significant reduction in power rating of converters. With DPP converters, a fraction of power generated by unshaded substrings is transferred to shaded ones so that characteristics of all substrings are virtually unified even under partial shading conditions.

Various kinds of DPP converters have been proposed and developed to enhance the energy yield of PV panels under partial shading. Nonisolated bidirectional PWM converters [4]–[10] are the most straightforward topology, through which neighboring substrings exchange power depending on shading conditions. Single-input–multi-output converters, such as multi-winding flyback converter [11], multi-stacked buck-boost converters [12], [13], and resonant voltage multiplier [14], [15], offer simpler circuit with reduced switch count. Isolated bidirectional flyback converters allow flexible power transfer even between remote substrings [16]–[19].

Among the most promising and viable DPP converter topologies is a switched capacitor converter (SCC) [20]–[23]. In addition to their simple circuit and simple operation principle, SCCs are advantageous over any other DPP converters in terms of circuit volume because of the superior energy density of capacitors over inductors—energy densities of discrete capacitors are in the range of three orders of magnitude of those of similarly-scaled inductors [24], [25].

Although most DPP converters have been proposed for substring-level power balancing, the DPP concept can be

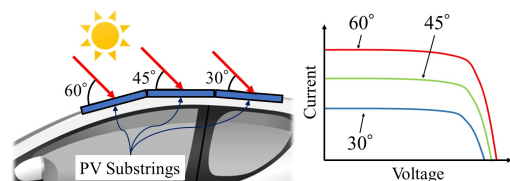


Fig. 1. Image of uneven irradiance and mismatched substring characteristics in solar roof for PHEVs.

M. Uno and Y. Saito are with the College of Engineering, Ibaraki University, Hitachi 316-8511, Japan (e-mail: masatoshi.uno.ee@vc.ibaraki.ac.jp).

S. Urabe is with Toyota Motor Corporation, Shizuoka, Japan (e-mail: shinichi_urabe_aa@mail.toyota.co.jp).

M. Yamamoto is with SEIKO EPSON Corporation, Nagano, Japan (e-mail: saya0460@gmail.com).

applied to any granularity levels, including cell-level power balancing. The finer the granularity level, the greater will be the energy yield under partial shading conditions [1], [5], [26]. Cell-level DPP architectures, however, require numerous converters in proportion to the cell count and therefore are unpractical unless DPP converters are dramatically simplified and miniaturized.

To achieve an even simpler and more compact circuit, the capacitorless SCC-based cell-level diffusion charge redistribution (DCR) converter utilizing diffusion capacitance of PV cells has been proposed, as shown in Fig. 2 [27], [28]. A diffusion capacitance C_d , a parasitic element originating from a P-N junction of PV cells (see the inset of Fig. 2), is used as a capacitor of SCCs, achieving even simpler and more compact circuit design by eliminating discrete capacitors. The conventional capacitorless cell-level DCR converter, however, has to keep its switching operation even when cell characteristics are perfectly matched under unshaded conditions, naturally increasing losses associated with pulsating currents generated by switching operations. In addition to the efficiency penalty under unshaded conditions, this conventional capacitorless DCR converter is only applicable to modules comprising odd number cells, likely limiting its applications because most standard PV modules consist of even number cells (e.g., 36, 60, and 72 cells).

This paper proposes a novel PWM SCC-based DCR converter utilizing diffusion capacitance of PV cells—this paper presents the extended work of [29]. Although an extra discrete capacitor and inductor are necessary, Joule losses associated with the DCR converter can be reduced especially under unshaded conditions, in comparison with the conventional DCR converter [27], [28]. In addition, the proposed DCR converter consists of even number cells and therefore would be easily applied to standard PV panels. The loss of the DCR converter is significantly dependent on shading conditions, and its duty cycle should be properly adjusted in order to minimize the loss. To this end, a novel dual MPPT technique, which controls duty cycles of not only the DCR converter but also an external front-end boost converter, is also proposed in this paper.

The rest of this paper is organized as follows. Section II presents the measurement of the diffusion capacitance of PV cells. Section III describes the topology of the proposed DCR converter and its major features. Detailed analysis will be performed in Section IV, followed by the theoretical loss comparison in Section V. Section VI introduces the novel dual MPPT control technique for the proposed DCR converter, followed by experimental verification tests in Section VII.

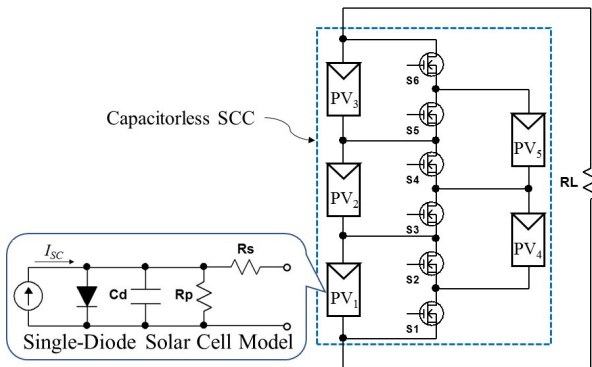


Fig. 2. Conventional capacitorless SCC-based DCR converter utilizing diffusion capacitance of PV cells.

II. MEASUREMENT OF DIFFUSION CAPACITANCE OF PV CELL

Before detailing the proposed DCR converter, the measurement results of the diffusion capacitance of actual PV cells are reported in this section.

A. Experimental Setup

AC impedance, or Nyquist plot, of a mono-crystalline silicon PV cell with 125×125 mm and an efficiency of approximately 20% (C60 Solar Cell, Sunpower) [30] was measured on the basis of ac impedance spectroscopy using a frequency response analyzer (FRA5087, NF Corporation). The measurement was performed outdoors under various irradiance conditions, including zero-irradiance conditions (i.e., dark $I-V$ conditions). The experimental setup is shown in Figs. 3(a) and (b). Irradiance was measured using a pyranometer (ES-602, EKO). Under the dark $I-V$ conditions, the cell was covered with a black box to completely shut off lights. The excitation signal from the FRA was applied to an electronic load (PLZ70UA, Kikusui Electronic) to draw ac currents superimposed on a dc current. Under dark $I-V$ conditions, a bipolar power supply (HSA4012, NF Corporation) was employed instead of the electronic load because of no current generated by the cell—a current source/sink is necessary to measure an ac impedance under dark $I-V$ conditions. The current of the PV cell was measured using a current probe (TCPA300, Tektronics). The excitation signal was swept in the frequency range of 1 Hz–100 kHz at various bias voltages V_{bias} .

From the measured Nyquist plots, the diffusion capacitance C_d was calculated. A typical Nyquist plot of a PV cell is depicted in Fig. 3(c). The semi-circle represents a time constant formed by a parallel resistance R_p and C_d . From the diameter (i.e., R_p) and a frequency at the vertex f_{cnr} , C_d can be determined as

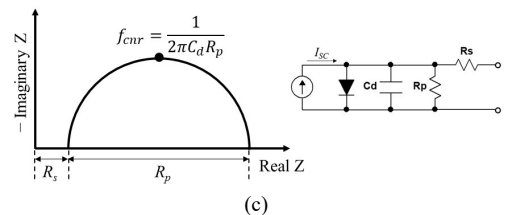
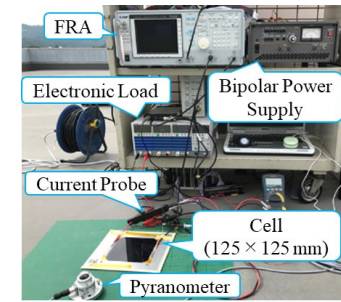
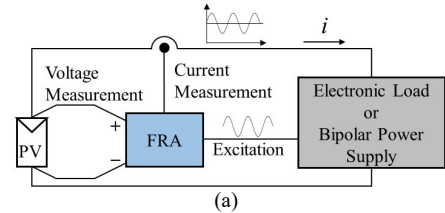


Fig. 3. Experimental setup for diffusion capacitance measurement. (a) Schematic diagram. (b) Photograph of measurement system outdoors. (c) Typical Nyquist plot of PV cell.

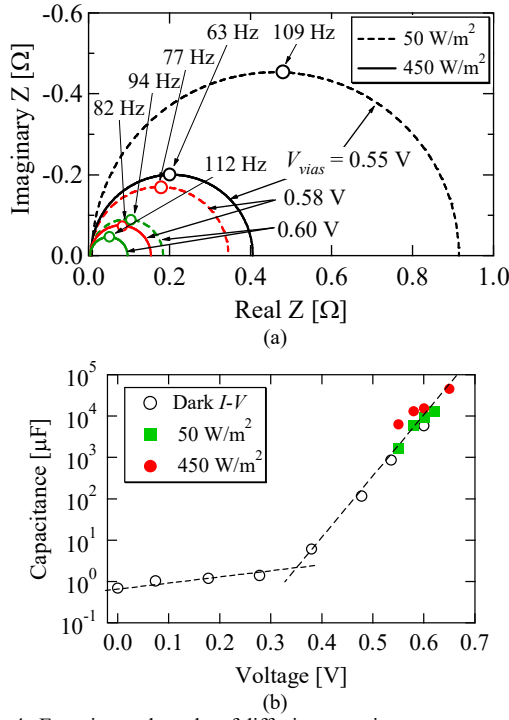


Fig. 4. Experimental results of diffusion capacitance measurement. (a) Nyquist plots. (b) Diffusion capacitance vs. bias voltage.

$$f_{cnr} = \frac{1}{2\pi C_d R_p}. \quad (1)$$

B. Measured Diffusion Capacitance

Measured Nyquist plots are shown in Fig. 4(a). The measured plots were dependent on V_{bias} and irradiance. The diameters of the semi-circles increased at low irradiance and low V_{bias} .

The calculated C_d from the obtained Nyquist plots are shown in Fig. 4(b). The values of C_d exhibited a significant dependence on V_{bias} , whereas the irradiance dependence was very minor. The calculated C_d showed an inflection point around $V_{bias} = 0.35$ V, and similar tendencies were reported in the previous work [31]. The calculated values of C_d at the maximum power point voltage of about 0.574 V were greater than 6.0 mF. These calculated C_d values were in a range of more than two orders of magnitude over those reported in [32], [33]. In general, C_d is proportional to a carrier lifetime τ and cell area (or short-circuit current), and Kim et al. reported C_d of around 20 μ F for the poly-crystalline PV cell (152×152 mm) with τ of 6.5×10^{-7} sec [32]. C_d of a silicon PV cell (20×40 mm) with τ of 4.12×10^{-5} sec is reportedly around 100 μ F at 0.43 V [31], and high-efficiency cells exhibit much longer τ of 6.0×10^{-5} – 1.6×10^{-4} sec [34], which is greater than two orders of magnitude of that reported in [32]. Although τ of the tested cell in this paper is unknown, given the reported values of τ and C_d per unit area in [31], [34], the calculated values of C_d in Fig. 4(b) are considered to be in a plausible range. C_d of 6.0 mF was considered sufficiently large to be used as capacitors of SCC-based DCR converters.

III. PROPOSED PWM SCC-BASED DCR CONVERTER UTILIZING DIFFUSION CAPACITANCE OF PV CELLS

A. Circuit Description

The proposed PWM SCC-based cell-level DCR converter utilizing diffusion capacitance of PV cells is shown in Fig. 5,

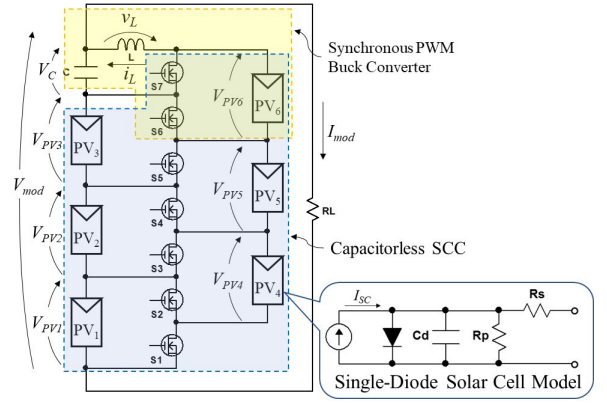


Fig. 5. Proposed PWM SCC-based DCR converter utilizing diffusion capacitance of PV cells.

in which diffusion capacitances are not illustrated for the sake of simplicity, except in the inset. A discrete inductor L and capacitor C are added to the six-cell capacitorless SCC so that a synchronous PWM buck converter is formed in the circuit. In other words, the proposed DCR converter is essentially the combination of the six-cell capacitorless SCC and synchronous PWM buck converter. The addition of the PWM buck converter achieves reduced losses, especially when cell characteristics are matched under unshaded conditions, in comparison with the conventional capacitorless DCR converter, as will be compared in Section V. It should be noted that the synchronous PWM buck converter in Fig. 5 is a floating one as PV_6 does not share a common line with C . The discrete capacitor C and the diffusion capacitance of PV_6 correspond to the output and input ports, respectively, of the synchronous PWM buck converter. Similar to the conventional capacitorless DCR converter, diffusion capacitances of cells function as capacitors for SCC. Since a discrete inductor and capacitor are necessary for the PWM buck converter, the proposed topology is not completely capacitorless.

B. Major Features

Both the conventional and proposed DCR converters requires $n+1$ switches (n being the cell count in the DCR converter). However, since a discrete inductor L and capacitor C are additionally necessary, the proposed DCR converter is slightly larger, more expensive and complex than the conventional DCR converter. But the impact of the increased volume and cost due to these added discrete elements is considered infinitesimal as PV modules are far larger and costlier than these two added elements.

Similar to the conventional topology shown in Fig. 2, the odd- and even-numbered switches are alternately driven so that the DCR converter operates under partial shading conditions. In the ideal case, all capacitor voltages are automatically unified at any duty cycle. Under unshaded conditions, on the other hand, the DCR converter operates with 0% duty cycle (i.e., $d = 0$ where d is the duty cycle of even-numbered switches), realizing the 3-series–2-parallel configuration. No pulsating currents flow when $d = 0$, and hence losses associated with switching operations can be significantly reduced in comparison with the conventional DCR topology, as will be compared in Section V.

Another advantage is that the proposed DCR converter can be applied to PV modules consisting of an even number of cells. Although the topology shown in Fig. 5 is for six cells,

it can be scaled to the arbitrary even number cells by simply adding cells and switches. Since most PV panels comprise even number cells (e.g., 60 and 72), the proposed DCR converter would be more suitable than conventional one which is applicable to odd number cells.

C. Proposed DCR Converter in PV Systems

Various DPP converter architectures have been proposed, such as adjacent module-to-module [4]–[10], [20]–[22], string-to-module [11]–[15], and module-to-bus [16]–[18] architectures, as shown in Fig. 6. The proposed and conventional DCR converters are roughly categorized into the adjacent module-to-module architecture, though these are a cell-level topology. Switches in the module-to-module (or cell-to-cell) architecture [see Fig. 6(a)] are rated based on module (or cell) voltage rather than string or bus voltage, hence lowering the cost and allowing for scalability. However, since the power transfer is limited only between adjacent two modules, the power of unshaded modules may have to traverse multiple converters before reaching shaded module(s). Therefore, a power conversion loss tends to collectively soar in systems comprising a lot of modules connected in series. In the string-to-module and module-to-bus architectures [see Figs. 6(b) and (c)], switch voltage rating needs to be as high as string or bus voltage, but the direct power conversion between shaded module(s) and string or bus allows reduced collective power conversion loss.

Kim et al. investigated the effects of scaling on the converter rating of the module-to-module and module-to-bus architectures [35]. The results revealed that the module-to-module architecture has a lower converter rating in small-scale systems comprising less than eight modules, while the module-to-bus architecture can have a lower rating in large-scale systems. The reported results suggest that the proposed DCR converter should not be applied to panels comprising a large number of cells.

Modularized architectures combining cell- and module-level DPP converters would be a viable application of the proposed DCR converter, as shown in Fig. 6(d)—modularized architectures have already become common in

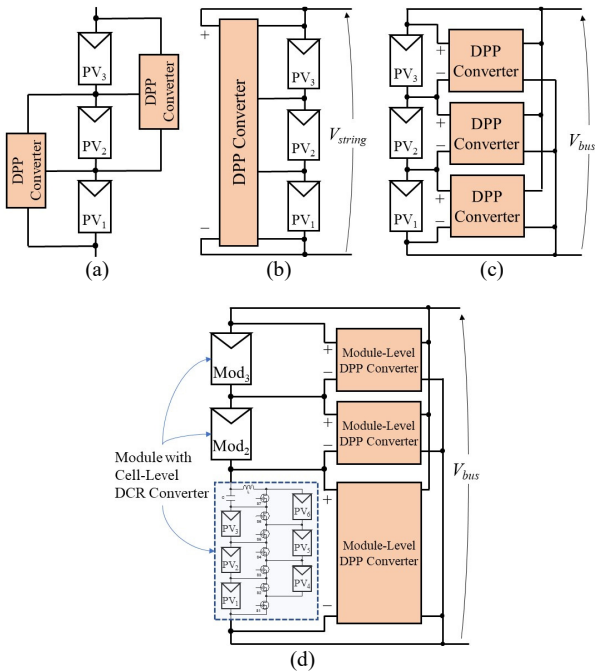


Fig. 6. DPP converter architectures. (a) Adjacent module-to-module architecture. (b) String-to-module architecture. (c) Module-to-bus architecture. (d) Modularized architecture.

battery equalization systems [36]–[38]. Cell-level DCR converters handle a limited number of cells (e.g., less than eight cells) in each module to avoid the issues of collective power conversion loss and increased converter rating. Meanwhile, module-level DPP converters are also applied for module-level power balancing. This modularized architecture is considered compatible with solar roofs for Prius PHEVs that consist of seven substrings each containing eight cells.

IV. OPERATION ANALYSIS

A. Voltage Conversion Ratio

The added capacitor C and PV_6 correspond to an output and input of the PWM buck converter in the proposed DCR converter, as can be seen from Fig. 5. Therefore, assuming all the cell voltages are ideally equal to V_{PV} , the voltage of C , V_C , is given by

$$V_C = dV_{PV}, \quad (2)$$

where d is the duty cycle of even-numbered switches. The voltage of a module consisting of n cells (n is an even number) is generalized as

$$V_{mod} = \left(\frac{n}{2} + d\right)V_{PV}. \quad (3)$$

Hence, for the module consisting of six cells ($n = 6$) shown in Fig. 5, $V_{mod} = (3 + d)V_{PV}$. This equation suggests that module characteristics seen from the output are dependent on d . In other words, I - V and P - V characteristics of the module seen from the output terminal change with d .

B. Charge Vector Analysis

Diffusion capacitances in the proposed DCR converter deliver a unique amount of charge, depending on their positions, d , and shading conditions. The mathematical analysis based on the charge vector analysis [39]–[41] is performed to compare the conventional and proposed DCR converters quantitatively. To simplify the analysis, a diode

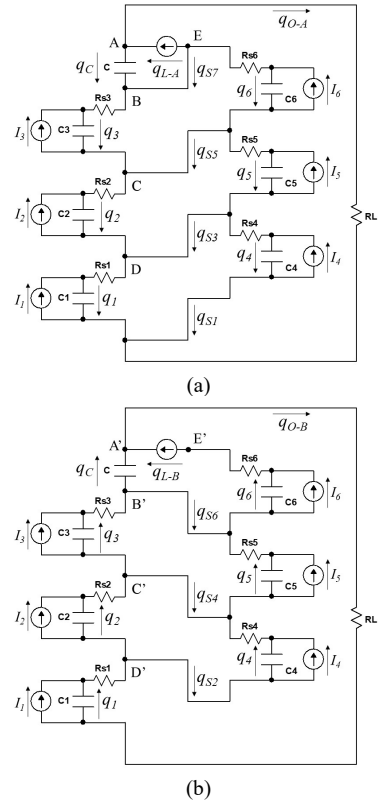


Fig. 7. Operation modes. (a) Mode A. (b) Mode B.

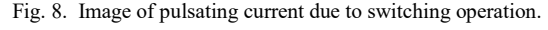
The operation modes of the proposed SCC-based DCR converter are shown in Fig. 7, in which the inductor L is equivalently illustrated as a current source. By defining charge flows in each mode as designated in Fig. 7, the Kirchhoff's current law (KCL) at nodes A–D in Mode A [see Fig. 7(a)] yields the following set of equations;

where $d' = (1 - d)$. Similarly, from the KCL at Nodes A'–E' in Mode B [see Fig. 7(b)],

The charge delivered through L is proportional to the mode length, and therefore,

For the sake of convenience, the voltage of the load resistor R_L is assumed constant, so is the sum voltage of C_1 – C_3 and C . Neglecting voltage drops across R_{s1} – R_{s3} gives

Equations (4)–(7) can be arranged in the matrix form as shown at the bottom of this page. The last six elements in the column vector on the left-hand side refer to currents of cells, I_1 – I_6 . For example, $[1, 1, 1, 1, 1, 1]^T$ means that all of I_1 – I_6 are 1.0 A (i.e., $[I_1, I_2, I_3, I_4, I_5, I_6]^T = [1, 1, 1, 1, 1, 1]^T$). Arbitrary values can be applied to the last six elements to emulate mismatched partial shading conditions as will be exemplified in Section V. From this matrix, the unique amount of charge delivered in each operation mode can be determined. The equations and matrix obtained in this subsection do not contain diffusion capacitance C_d , indicating that the charge amount flowing in the circuit is independent on C_d . The determined charge amount will be used to derive losses of switches and cells, in the following subsections.



In general, SCC operations can be characterized by two asymptotic limits of slow switching limit (SSL) and fast switching limit (FSL). A rough boundary between the SSL and FSL is whether the switching frequency f_s is higher or lower than a corner frequency f_c that is the inverse of a product of capacitance and resistance [42]— $f_s > f_c$ in FSL, and vice versa in SSL. Given that the measured C_d of approximately 6.0 mF (see Section II-B) and prototype's total effective resistance of approximately 30 m Ω [a switch on-resistance of 13.4 m Ω , cell series resistance R_s of 5.0 m Ω (see Tables I and II), and cable resistance of approximately 10 m Ω], f_c is determined to be 5.6 kHz. Since experiments were performed at f_s of 15 kHz, the SCC was assumed to operate in the FSL region; details about the prototype and experiments will be described in Section VII. Although SSL operations should also be considered for a correct calculation, the FSL operation only is considered to simplify the analysis in this section.

The superimposed ac component naturally increases an RMS current as well as the Joule loss to some extent. The charge flowing through R_{si} in Modes A and B, $q_{Rsi,A}$ and $q_{Rsi,B}$, are expressed as

$$\begin{bmatrix} 0 \\ 0 \\ 0 \\ 0 \\ 0 \\ 0 \\ 0 \\ 0 \\ 0 \\ 0 \\ 1 \\ 1 \\ 1 \\ 1 \\ 1 \\ 1 \\ 1 \end{bmatrix} = \begin{bmatrix} 0 & 0 & 0 & 0 & 0 & -1 & 1 & 0 & -1 & 0 & 0 & 0 & 0 & 0 & 0 & 0 & 0 \\ 0 & 0 & -1 & 0 & 0 & -1 & 1 & -1 & 0 & 0 & 0 & 0 & d' & 0 & 0 & -d' & 0 \\ 0 & 0 & -1 & 1 & 0 & -1 & 1 & 0 & 0 & 0 & 0 & 0 & d' & -d' & 0 & d' & -d' \\ -1 & 1 & 0 & -1 & 1 & 0 & 0 & 0 & 0 & 0 & 0 & d' & -d' & 0 & d' & -d' & 0 \\ 0 & 0 & 0 & 0 & 0 & 0 & 1 & 0 & 1 & 0 & -1 & 0 & 0 & 0 & 0 & 0 & 0 \\ 0 & 0 & 0 & 1 & 0 & 1 & -1 & -1 & 0 & 0 & 0 & 0 & 0 & d & 0 & d & -d \\ 0 & 0 & 1 & -1 & 1 & -1 & 0 & 0 & 0 & 0 & 0 & 0 & d & -d & d & -d & 0 \\ 0 & 1 & -1 & 0 & -1 & 0 & 0 & 0 & 0 & 0 & 0 & d & -d & 0 & -d & 0 & 0 \\ 0 & 0 & 0 & 0 & 0 & 0 & 0 & 0 & d & -d' & 0 & 0 & 0 & 0 & 0 & 0 & 0 \\ 0 & 1 & 1 & 1 & 0 & 0 & 0 & 1 & 0 & 0 & 0 & 0 & 0 & 0 & 0 & 0 & 0 \\ 0 & 0 & 0 & 0 & 0 & 0 & 1 & 0 & 0 & -1 & 0 & 0 & 0 & 0 & 0 & 0 & 0 \\ 0 & 0 & 0 & 0 & 0 & 0 & 0 & 0 & 0 & 0 & 0 & 1 & 0 & 0 & 0 & 0 & 0 \\ 0 & 0 & 0 & 0 & 0 & 0 & 0 & 0 & 0 & 0 & 0 & 0 & 0 & 1 & 0 & 0 & 0 \\ 0 & 0 & 0 & 0 & 0 & 0 & 0 & 0 & 0 & 0 & 0 & 0 & 0 & 0 & 1 & 0 & 0 \\ 0 & 0 & 0 & 0 & 0 & 0 & 0 & 0 & 0 & 0 & 0 & 0 & 0 & 0 & 0 & 1 & 0 \\ 0 & 0 & 0 & 0 & 0 & 0 & 0 & 0 & 0 & 0 & 0 & 0 & 0 & 0 & 0 & 0 & 1 \end{bmatrix} \begin{bmatrix} q_1 \\ q_2 \\ q_3 \\ q_4 \\ q_5 \\ q_6 \\ q_C \\ q_{L,A} \\ q_{L,B} \\ q_{O,A} \\ q_{O,b} \\ I_1 \\ I_2 \\ I_3 \\ I_4 \\ I_5 \\ I_6 \end{bmatrix} \quad (8)$$

$$\begin{cases} q_{R_{Si}.A} = -q_i + d'I_i \\ q_{R_{Si}.B} = q_i + dI_i \end{cases} \quad (9)$$

Currents of R_{Si} in Modes A and B are

$$\begin{cases} I_{R_{Si}.A} = \frac{q_{R_{Si}.A}}{d'} \\ I_{R_{Si}.B} = \frac{q_{R_{Si}.B}}{d} \end{cases} \quad (10)$$

The total Joule loss of R_{Si} , $P_{R_{Si}.tot}$, is

$$P_{R_{Si}.tot} = \sum_{i=1}^6 (d'I_{R_{Si}.A}^2 + dI_{R_{Si}.B}^2) R_{Si}. \quad (11)$$

This equation suggests that the Joule loss of R_{Si} is independent on C_d .

Cells generate Joule losses in the form of $I_i^2 R_{Si}$ when without the DCR converter. Joule losses due to pulsating currents, $P_{R_{Si}.tot.p}$, can be expressed as

$$P_{R_{Si}.tot.p} = P_{R_{Si}.tot} - \sum_{i=1}^6 I_i^2 R_{Si}, \quad (12)$$

where the second term on the right-hand side is the Joule loss in the case without the DCR converter.

D. Joule Loss of Switches

Unique amount of charge flowing through switches can be similarly determined from Figs. 7(a) and (b), as

$$\begin{cases} q_{S1} = q_4 - d'I_4 \\ q_{S2} = q_4 + dI_4 \\ q_{S3} = -q_4 + q_5 + d'(I_4 - I_5) \\ q_{S4} = q_2 - q_3 + d(I_2 - I_3) \\ q_{S5} = -q_5 + q_6 + d'(I_5 - I_6) \\ q_{S6} = q_3 - q_C + dI_3 \end{cases} \quad (13)$$

Switch current, i_{Si} ($i = 1 \dots 7$), is expressed as

$$i_{Si} = \begin{cases} \frac{q_{Si}}{d'} & (i = 1, 3, 5, 7) \\ \frac{q_{Si}}{d} & (i = 2, 4, 6) \end{cases} \quad (14)$$

The total Joule loss of switches, $P_{S.tot}$, is given by

$$P_{S.tot} = R_{on} \left(\sum_{i=1,3,5,7} d'i_{Si}^2 + \sum_{i=2,4,6} di_{Si}^2 \right), \quad (15)$$

where R_{on} is the on-resistance of switches. Similar to the Joule loss of the series-resistance R_{Si} in the previous subsection, C_d does not appear in (15) and has no influence on the switch Joule loss.

V. LOSS COMPARISON WITH CONVENTIONAL CAPACITORLESS DCR CONVERTERS

Based on the derived Joule loss models in the previous section, the total Joule losses of the proposed DCR converter

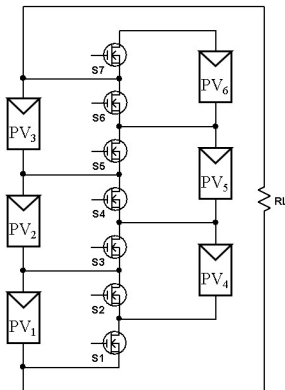


Fig. 9. Capacitorless DCR converter comprising six cells.

TABLE I
PARAMETERS USED FOR QUANTITATIVE LOSS COMPARISON

Switching Frequency, f_s	15 kHz
Series Resistance, R_{Si}	5.0 mΩ
On-Resistance, R_{on}	13.4 mΩ
ESR of Inductor, r_L	3.6 mΩ
ESR of Capacitor, r_C	1.0 mΩ

are compared with those of the conventional capacitorless topology shown in Fig. 2. In addition, the capacitorless DCR converter comprising six cells (see Fig. 9) is also included for the loss comparison. Parameters used for the comparison are listed in Table I. In this comparison, all cells generate 5.0 A (i.e., $[I_1, I_2, I_3, I_4, I_5, I_6]^T = [5, 5, 5, 5, 5, 5]^T$), and total losses are normalized by the number of cells in each circuit because the proposed and conventional DCR converters contain different numbers of cells;

$$\text{Normalized Loss} = \frac{\text{Total Loss}}{\text{Number of Cells}}. \quad (16)$$

Theoretical normalized Joule losses under the unshaded condition are compared in Fig. 10. Switching losses, which are roughly expressed as $\frac{1}{6} V_{PV} i_{Si} f_s (T_{rise} + T_{fall})$ (f_s , T_{rise} , and T_{fall} being the switching frequency, rise time, and fall time, respectively), were also calculated based on the determined current values of (14). The calculated switching losses were lower than 0.01 W/cell for all three DCR converter topologies chiefly because nominal cell voltages were lower than 0.6 V. The switching losses were negligibly small in cell-level DCR converters and therefore are not

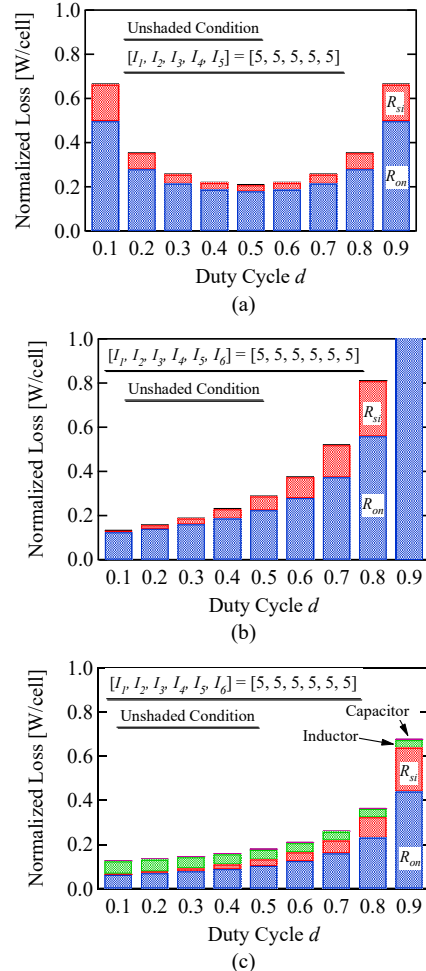


Fig. 10. Normalized Joule losses as a function of duty cycle d under unshaded condition: (a) conventional capacitorless five-cell DCR, (b) six-cell DCR, (c) proposed DCR converter.

included in the loss comparison. The Joule loss due to the discrete capacitor C in the proposed DCR converter was also negligibly small thanks to the low ESR of C . The normalized Joule losses in the conventional capacitorless five-cell DCR converter became lowest at $d = 0.5$, as shown in Fig. 10(a), because of its symmetric circuit (see Fig. 2). The capacitorless six-cell DCR and proposed DCR converters, on the other hand, showed different tendencies that the losses decreased at small d , as shown in Figs. 10(b) and (c). As d neared 0, the Joule loss of cells disappeared because the operation of $d = 0$ was equivalent to the 3-series–2-parallel configuration, as discussed in Section III—note that Joule losses of R_{si} associated only with ac current components due to switching operations were considered in order to fairly compare the losses of DCR converters [see (12)]. The losses in R_{si} of the conventional capacitorless six-cell DCR converter were rather larger than those of the proposed converter. This is chiefly because PV_6 in Fig. 9 is open-circuited during even-numbered switches are on, hence resulting in larger current pulsation in R_{si6} .

Calculated normalized losses under the shaded condition of $[I_1, I_2, I_3, I_4, I_5, I_6]^T = [2.5, 5, 5, 5, 5, 5]^T$ are shown in Fig. 11— PV_1 was partially-shaded and its short-circuit current was half those of other unshaded cells. Losses under shaded conditions were larger than those under the unshaded condition for all topologies because of the relatively large power transfer among cells for power balancing. More importantly, the duty cycle achieving the lowest loss under shaded conditions in Fig. 11 differed from those under the

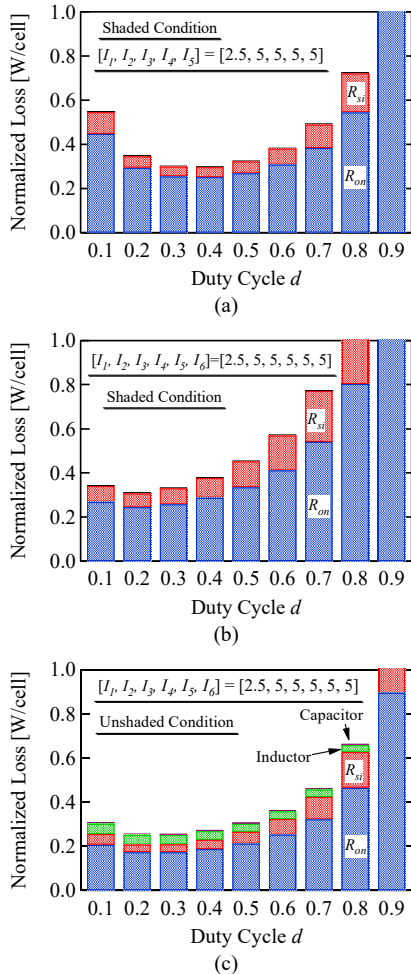


Fig. 11. Normalized Joule losses as a function of duty cycle under shaded conditions: (a) conventional capacitorless five-cell DCR, (b) six-cell DCR, (c) proposed DCR converter.

unshaded conditions of Fig. 10. These results suggest that the optimal duty cycle for the lowest Joule loss varies depending on shading conditions and that the duty cycle should be properly adjusted in order to minimize the losses.

In the next section, a novel dual MPPT control algorithm is proposed to realize the optimal duty cycle operation and to minimize the Joule losses of the proposed SCC-based DCR converter.

VI. DUAL MPPT CONTROL

A module characteristic with the proposed DCR converter varies depending on duty cycle d as (3) indicates; the module voltage increases with d . In addition, an optimal duty cycle d for the lowest Joule loss is dependent on shading conditions, as discussed in the previous section. It should be noted that a module's operating point cannot be determined with d but an external circuit that is usually a boost converter for ordinary PV panels. In other words, a PV module with the proposed PWM SCC-based DCR converter operates in conjunction with an external front-end boost converter.

A dual MPPT technique manipulating not only duty cycle d of the proposed DCR converter but also duty cycle D of an external front-end boost converter is proposed so that the module can operate at its MPP with minimizing Joule losses. The control block diagram is illustrated in Fig. 12(a). The dual MPPT control system consists of two feedback loops. V_{mod} and I_{mod} are measured to calculate P_{mod} , and both d and D are simultaneously manipulated to maximize P_{mod} . To decouple two MPPT control loops, a sampling interval of MPPT for d should be approximately 10 times greater than

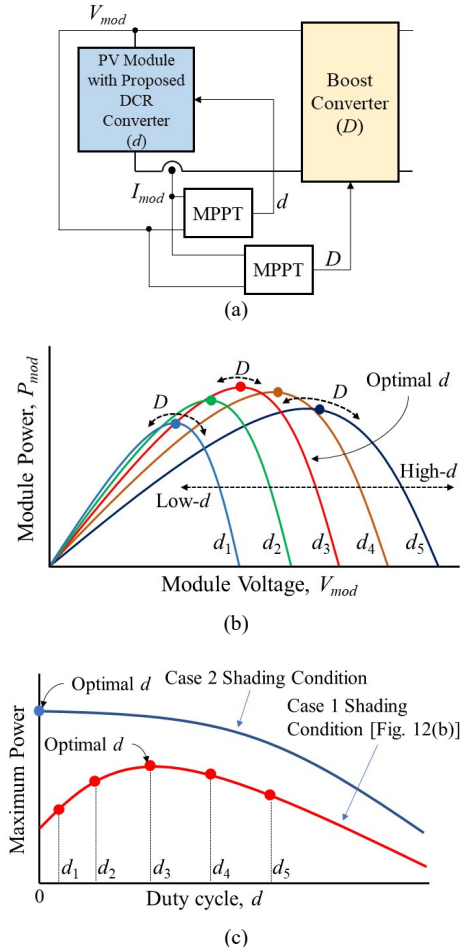


Fig. 12. (a) Dual MPPT control block diagram. (b) Notional module characteristics with dual MPPT control under shaded condition. (c) Maximum power vs. duty cycle d of DCR converter.

that for D . Ordinary MPPT algorithms, such as P&O, incremental conductance, etc., can be employed for both control loops for the proposed dual MPPT control.

Notional module characteristics with the proposed dual MPPT control are depicted in Fig. 12(b). An optimal module characteristic is sought by the DCR converter adjusting d while an MPP is tracked by the boost converter manipulating its duty cycle D . Module characteristics seen from the boost converter are dependent on d , as indicated by (3). More importantly, the extractable maximum power is also dependent on d and shading conditions because the optimal duty cycle d of the DCR converter for the lowest loss varies depending on shading conditions, as discussed in Section V. In the case of Fig. 12(b), the optimal duty cycle is d_3 .

Figure 12(c) illustrates notional characteristics of maximum power vs. duty cycle d under two shading conditions: Case 1 is a heavily-shaded condition, which corresponds to the case in Fig. 12(b), and Case 2 is a lightly-shaded or unshaded condition. Under Case 1 shading condition, for example, the largest maximum power is obtained at d_3 , and the maximum power decreases as d moves away from d_3 . Hence, the characteristic of the maximum power is convex. Under the Case 2 shading condition, on the other hand, the optimal d is zero, at which the loss is minimized and the PV module is equivalent to the 3-series–2-parallel configuration (see Section III-B). The maximum power monotonically decreases with d under Case 2 shading condition. Thus, the shapes of these characteristics vary depending on shading conditions, and d needs to be properly adjusted to extract the maximum power accordingly.

VII. EXPERIMENTAL RESULTS

A. Prototype

A prototype of the DCR converter for six cells was built, as shown in Fig. 13, and its circuit elements are listed in Table II. The prototype was designed for proof-of-concept, not for practical use, and its voltage was even lower than 2.5 V. To drive the MOSFETs with the gate threshold voltage

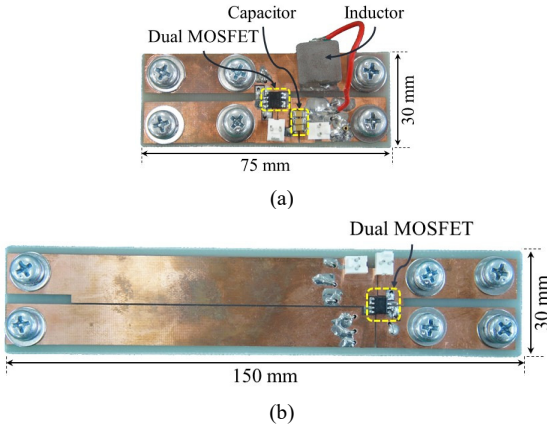


Fig. 13. Photograph of the proposed DCR converter prototype. (a) End board. (b) Extension board.

TABLE II
CIRCUIT ELEMENTS USED FOR PROTOTYPE

Element	Value
Switches	Dual MOSFET, IFR9910, $V_{GS(th)} = 2.55$ V $R_{on} = 13.4$ m Ω (low-side) and 9.3 m Ω (high-side)
Gate Driver	ISL6596
L	10 μ H, 3.6 m Ω
C	Ceramic Capacitor, 300 μ F, 1.0 m Ω

$V_{GS(th)}$ of 2.55 V (see Table II), external isolated ac-dc converters (DRL10-12-1, TDK Lambda) with an output voltage of 5.0 V were used to power the gate drivers. A modular design was employed, and the prototype consisted of an end board and three extension boards. The inductor and capacitor were mounted on the end board. Each extension board contains two switches (dual MOSFET, IFR9910) and a gate driver for two cells. This modular design allows the number of cells can be arbitrarily increased by stacking extension boards. The size of extension boards was determined to be slightly larger than that of cells so that wiring cables be as short as possible. The end and extension boards were directly connected using screws.

PV cells (125×125 mm) with a diffusion capacitance of approximately 6.0 mF at its MPP voltage [see Fig. 4(b)] were used. The DCR converter was operated at f_s of 15 kHz.

B. Module Characteristics with/without DCR Converter

Module characteristics with/without the proposed DCR converter were measured without connecting a boost converter. The field testing for the characteristic measurement was carried out at 15:50 on August 17, 2017, in Hitachi, Japan. To emulate a partial shading condition, half of PV₁ was covered with a postcard so that its short-circuit current was reduced to half those of other cells. Under this partial shading condition, an electronic load was directly connected to the module to manually sweep module characteristics, while d of the DCR converter was fixed to be 0.1. As a reference, a characteristic of a module comprising six cells connected in series with traditional bypass diodes was also measured under the same shading condition.

The measured module characteristics with/without the DCR converter are shown and compared in Fig. 14. The characteristic with bypass diodes exhibited two power point maxima (one global and one local MPPs), and its maximum power was merely 5.38 W at the irradiance of 455 W/m². With the DCR converter, on the other hand, the local MPP disappeared, and the maximum power increased to as high as 7.73 W at the irradiance of 471 W/m². These results correspond to 36% improvement in the maximum power against the percentage increase of 3.5% in the irradiance, demonstrating the efficacy of the proposed DCR converter.

C. Comparison with Conventional Six-Cell DCR Converter

Module characteristics with/without the end board were measured at various duty cycle d without connecting a boost converter. The DCR converter without the end board is equivalent to the conventional six-cell DCR topology shown in Fig. 9. Half of PV₅ was covered with a postcard to emulate a shading condition.

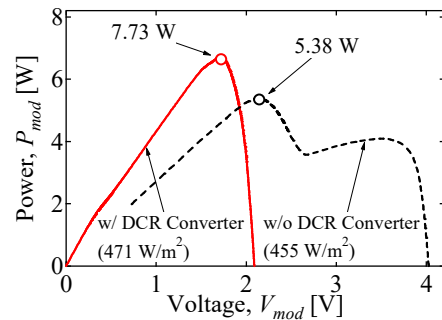


Fig. 14. Measured module characteristics with/without DCR converter at $d = 0.1$.

Characteristics of the shaded and unshaded reference cells are shown in Fig. 15(a). Maximum powers of the unshaded and shaded cells were 1.82 and 0.93 W, respectively. Measured representative P - V characteristics with $d = 0.3$ are shown in Fig. 15(b). There were no local MPPs observed in both characteristics, indicating that partial shading issues were successfully precluded. Extractable maximum powers as a function of duty cycle d are compared in Fig. 15(c). The observed tendencies were slightly different due to the different topology. The extractable maximum power of the proposed DCR converter was larger in the almost entire duty cycle range. Given that the measurement was performed under the nearly identical irradiance condition of 600 W/m^2 , the increased power yield by the proposed DCR converter

TABLE III
IRRADIANCE AND SHADING CONDITIONS FOR EXPERIMENTS

	Irradiance [W/m^2]	Partial Shading
Case A	785	30% of PV_2 and PV_5
Case B	600	50% of PV_5
Case C	880	50% of PV_5

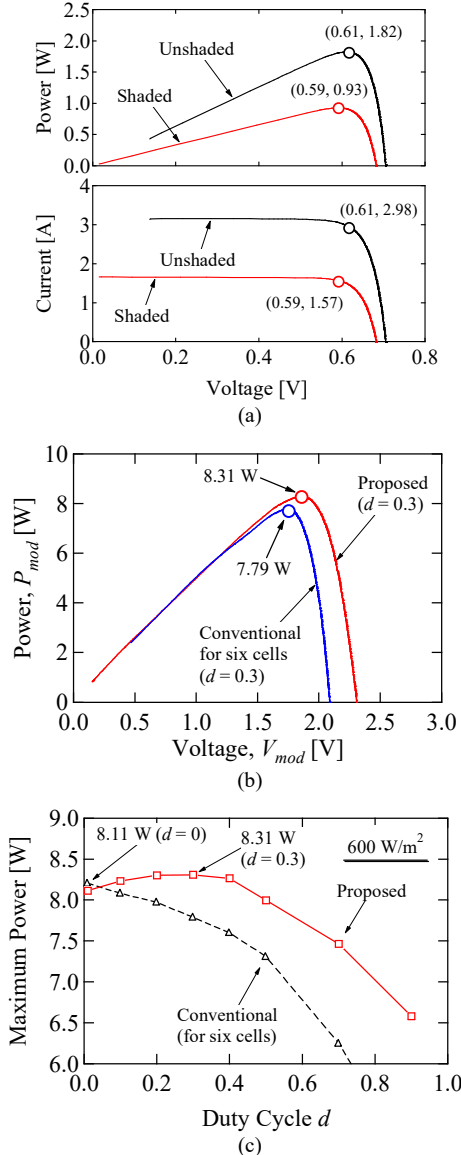


Fig. 15. (a) Reference cell characteristics. (b) Measured representative P - V characteristics with $d = 0.3$. (c) extractable maximum power as a function of duty cycle d of PV module with conventional and proposed DCR converters.

demonstrated the superior performance. The measured peak power of 8.31 W with $d = 0.3$ corresponds to an overall efficiency of 82.9%, which is a ratio of an extractable power to theoretical module power [= $8.31 \text{ W} / (1.82 \text{ W} \times 5 \text{ cells} + 0.93 \text{ W} \times 1 \text{ cell})$].

D. Influence of Partial Shading on Module Characteristics

As shown in the previous subsection, the extractable maximum power varied with d . To investigate the influence of shading conditions on characteristics of maximum power, similar experiments under three partial shading conditions of Cases A–C were performed outdoors. Partial shading and irradiance conditions in Cases A–C are summarized in Table III. Module characteristics with the DCR converter were manually swept at various duty cycles to grasp the d -dependent characteristics. As reference data, characteristics of shaded and unshaded reference cells were also measured.

Characteristics of the shaded and unshaded reference cells under Case A shading condition are shown in Fig. 16(a). Measured module characteristics are shown in Fig. 16(b). Measured characteristics varied depending on d , as (3) indicated—the open-circuit voltage of the module increased with d . More importantly, extractable maximum powers slightly varied with d .

The extractable maximum powers as a function of d in Cases A–C are compared in Fig. 17. The optimal range of d varied depending on shading conditions. For example, the maximum power in Case A peaked at $d = 0.3$ and decreased as d moved away from 0.3. This convex characteristic suggested that the optimal d existed in the range of $0.2 < d < 0.4$ under Case A shading condition. Similar convex characteristic was also observed in Case B. Meanwhile, the optimal d in Case C was 0. These results suggest optimal duty

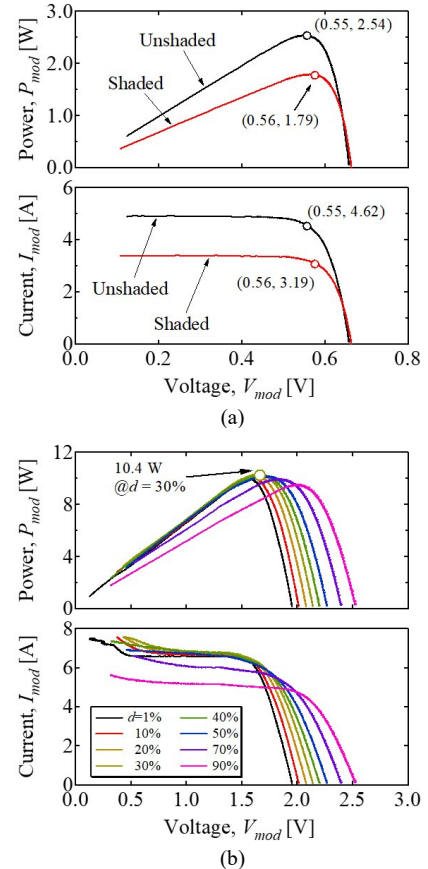


Fig. 16. Measured characteristics of (a) reference cells and (b) modules with DCR converter under Case A partial shaded condition.

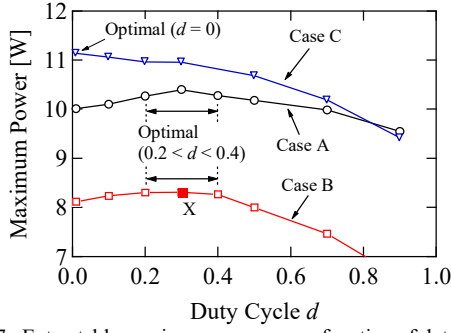


Fig. 17. Extractable maximum powers as a function of duty cycle d of PV module with DCR converter under partial shading conditions.

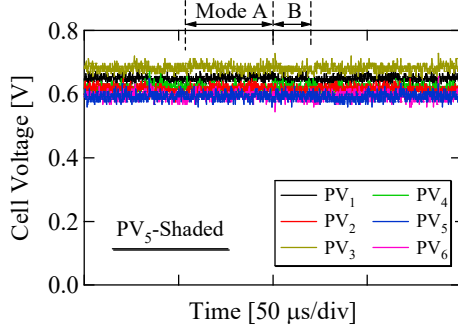


Fig. 18. Measured cell voltage under Case B partial shading condition.

cycle range vary depending on shading and irradiance conditions.

Cell voltages with $d = 0.3$ under Case B partial shading condition were measured when the module generated the maximum power (i.e., at the point X in Fig. 17), as shown in Fig. 18. Cell voltages were slightly imbalanced due to the nonideality of the DCR converter. All the cell voltages were nearly constant without noticeable voltage ripples. These measured cell voltage waveforms support the assumption that the proposed DCR converter operates in the FSL region, as discussed in Section IV-C.

E. Dual MPPT Control

The field testing for the dual MPPT control was performed to demonstrate the entire performance of the proposed DCR converter with its MPPT control strategy. The experimental setup for the dual MPPT control demonstration is shown in Fig. 19. Two cells, PV₂ and PV₅, were covered with postcards to emulate a partial shading condition—approximately 30% of these cells were covered, and this shading condition corresponds to Case A in Table III. The irradiance level during the testing was nearly constant as 785 W/m².

Hill-climbing MPPT algorithms were employed for both the DCR and boost converters. The boost converter operated with the duty cycle perturbation of $\Delta D = 1\%$ and a sampling

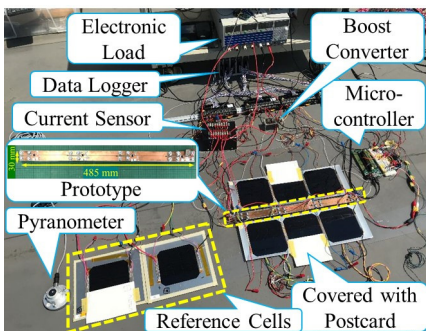


Fig. 19. Experimental setup for dual MPPT control.

interval of 100 ms. Meanwhile, MPPT conditions for the DCR converter were empirically determined as $\Delta d = 5\%$, and its sampling interval was set to be 1.0 s to decouple two MPPT control loops, as discussed in Section V. The DCR converter and boost converter were controlled using TMS320F28335 (Texas Instruments) control card, and V_{mod} and I_{mod} were recorded using a data logger (NR-500, KEYENCE).

The experimental results of the dual MPPT are shown in Fig. 20. The experiment was commenced from the initial duty cycles of $d = 0.25$ and $D = 0.4$, as shown in Fig. 20(a). D of the boost converter gradually rose up and P_{mod} increased. After D converged to the optimal point around $D = 0.73$, V_{mod} and I_{mod} fluctuated at nearly three levels in synchronization with D , similar to traditional hill-climbing MPPT algorithms. Meanwhile, d of the DCR converter also increased from the initial value of 0.25 and varied in the range of 0.30–0.45 after D reached the optimal point. After the operation came to the steady-state condition, P_{mod} reached approximately 10.2 W,

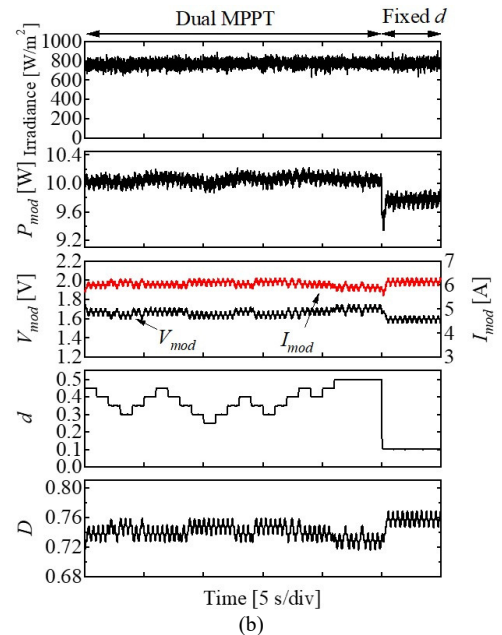
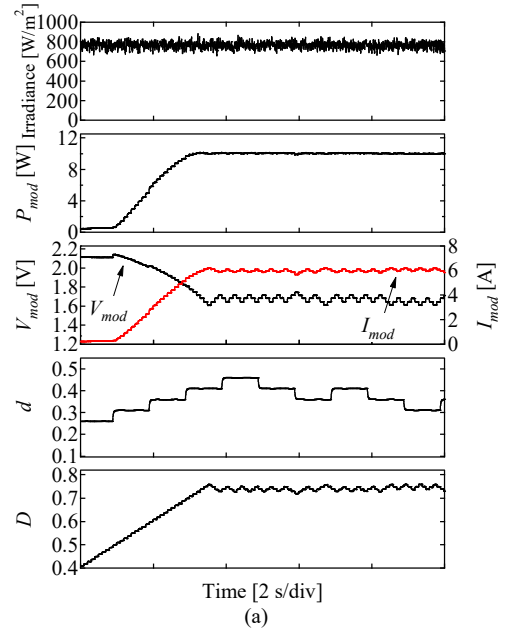


Fig. 20. Experimental results of dual MPPT control under partial shading condition. (a) From cold start. (b) At the moment when MPPT for the DCR converter was disabled.

as can be seen in Fig. 20(b). Given the slight weather change during the test, the measured P_{mod} and the variation range of d in Fig. 20 satisfactorily matched with the maximum P_{mod} of 10.4 W and the estimated optimal d of 0.2–0.4 in Fig. 16(b).

In order to accentuate the efficacy of the dual MPPT control, d was suddenly forced to be a fixed value of 0.1 [see the second panel from the bottom in Fig. 20(b)] to disable the dual MPPT control (i.e., the boost converter only operated with an MPPT control). P_{mod} abruptly dropped down as low as 9.8 W because the DCR converter did not track the optimal duty cycle. Thus, these results demonstrated the increased power yield by the proposed dual MPPT control.

VIII. CONCLUSION

The PWM SCC-based DCR converter utilizing diffusion capacitance of PV cells has been proposed for partially-shaded PV modules. The added discrete inductor and capacitor contribute to significantly reduce Joule losses associated with switching operations. In addition, the proposed DCR converter is applicable to modules comprising even number cells and is considered suitable from the viewpoint of practical implementation because most standard PV panels consist of even number cells.

AC impedance measurement based on the ac impedance spectroscopy using an FRA was performed for the PV cell with 125×125 mm, and the diffusion capacitance value was determined to be approximately 6.0 mF at its MPP voltage. The theoretical Joule loss model was derived based on the detailed operation analysis. The theoretical loss comparison between the proposed and conventional capacitorless DCR converters revealed that the proposed topology achieves lower losses and that the optimal duty cycle minimizing the Joule loss is dependent on shading conditions. The dual MPPT control technique was also proposed to minimize the Joule loss while tracking the MPP of the PV module employing the proposed DCR converter. With the dual MPPT control, the DCR converter operates with the optimal duty cycle minimizing the Joule loss, while the front-end boost converter seeks the MPP.

Experimental verification tests were performed for the modules comprising six cells. The local MPP successfully vanished, and the power yield from the module significantly improved compared to the case using traditional bypass diodes. With the dual MPPT control, the proposed DPP converter could operate with the optimal duty cycle to extract maximum power, demonstrating the proposed concepts.

REFERENCES

- [1] S. M. MacAlpine, R. W. Erickson, and M. J. Brandemuehl, "Characterization of power optimizer potential to increase energy capture in photovoltaic systems operating under nonuniform conditions," *IEEE Trans. Power Electron.*, vol. 28, no. 6, pp. 2936–2945, Jun. 2013.
- [2] M. Vitelli, "On the necessity of joint adoption of both distributed maximum power point tracking and central maximum power point tracking in PV systems," *Prog. Photovolt. Res. Appl.*, vol. 22, pp. 283–299, 2014.
- [3] R.C.N.P. Podgurski and D.J. Perreault, "Submodule integrated distributed maximum power point tracking for solar photovoltaic applications," *IEEE Trans. Power Electron.*, vol. 28, no. 6, pp. 2957–2967, Jun. 2013.
- [4] H. J. Bergveld, D. B  thker, C. Castello, T. Doorn, A. D. Jong, R. V. Otten, and K. D. Waal, "Module-level dc/dc conversion for photovoltaic systems: the delta-conversion concept," *IEEE Trans. Power Electron.*, vol. 28, no. 4, pp. 2005–2013, Apr. 2013.
- [5] M.S. Zaman, Y. Wen, R. Fernandes, B. Buter, T. Doorn, M. Dijkstra, H.J. Bergveld, and O. Trescases, "A cell-level differential power processing IC for concentrating-PV systems with bidirectional hysteretic current-mode control and closed-loop frequency regulation," *IEEE Trans. Power Electron.*, vol. 30, no. 12, pp. 7230–7244, Dec. 2015.
- [6] P.S. Shenoy, K.A. Kim, B.B. Johnson, and P.T. Krein, "Differential power processing for increased energy production and reliability of photovoltaic systems," *IEEE Trans. Ind. Power Electron.*, vol. 28, no. 6, pp. 2968–2979, Jun. 2013.
- [7] S. Qin, S.T. Cady, A.D.D. Garcia, and R.C.N.P. Podgurski, "A distributed approach to maximum power point tracking for photovoltaic submodule differential power processing," *IEEE Trans. Power Electron.*, vol. 30, no. 4, pp. 2024–2040, Apr. 2015.
- [8] S. Qin, C.B. Barth, and R.C.N.P. Podgurski, "Enhancing microinverter energy capture with submodule differential power processing," *IEEE Trans. Power Electron.*, vol. 31, no. 5, pp. 3575–3585, May 2016.
- [9] T. Shimizu, O. Hashimoto, and G. Kimura, "A novel high-performance utility-interactive photovoltaic inverter system," *IEEE Trans. Power Electron.*, vol. 18, no. 2, pp. 704–711, Mar. 2003.
- [10] T. Shimizu, M. Hirakata, T. Kamezawa, and H. Watanabe, "Generation control circuit for photovoltaic modules," *IEEE Trans. Power Electron.*, vol. 16, no. 3, pp. 293–300, May 2001.
- [11] J. Du, R. Xu, X. Chen, Y. Li, and J. Wu, "A novel solar panel optimizer with self-compensation for partial shadow condition," in *Proc. IEEE Applied Power Electron. Conf. Expo., APEC*, pp. 92–96, 2013.
- [12] M. Uno and A. Kukita, "Single-switch voltage equalizer using multi-stacked buck-boost converters for partially-shaded photovoltaic modules," *IEEE Trans. Power Electron.*, vol. 30, no. 6, pp. 3091–3105, Jun. 2015.
- [13] M. Uno and A. Kukita, "Current sensorless equalization strategy for a single-switch voltage equalizer using multistacked buck-boost converters for photovoltaic modules under partial shading," *IEEE Trans. Ind. Appl.*, vol. 53, no. 1, pp. 420–429, Jan./Feb. 2017.
- [14] M. Uno and A. Kukita, "Two-switch voltage equalizer using an LLC resonant inverter and voltage multiplier for partially-shaded series-connected photovoltaic modules," *IEEE Trans. Ind. Appl.*, vol. 51, no. 2, pp. 1587–1601, Mar./Apr. 2015.
- [15] M. Uno and A. Kukita, "Single-switch single-magnetic PWM converter integrating voltage equalizer for partially-shaded photovoltaic modules in standalone applications," *IEEE Trans. Power Electron.*, vol. 33, no. 2, pp. 1259–1270, Feb. 2018.
- [16] C. Olalla, D. Clement, M. Rodr  guez, and D. Maksimovi  , "Architectures and control of submodule integrated dc-dc converters for photovoltaic applications," *IEEE Trans. Power Electron.*, vol. 28, no. 6, pp. 2980–2997, Jun. 2013.
- [17] C. Olalla, C. Deline, D. Clement, Y. Levron, M. Rodr  guez, and D. Maksimovi  , "Performance of power limited differential power processing architectures in mismatched PV systems," *IEEE Trans. Power Electron.*, vol. 30, no. 2, pp. 618–631, Feb. 2015.
- [18] G. Chu, H. Wen, L. Jiang, Y. Hu, and X. Li, "Bidirectional flyback based isolated-port submodule differential power processing optimizer for photovoltaic applications," *Solar Energy*, vol. 158, pp. 929–940, Oct. 2017.
- [19] Y.T. Jeon, H. Lee, K.A. Kim, and J.H. Park, "Least power point tracking method for photovoltaic differential power processing systems," *IEEE Trans. Power Electron.*, vol. 32, no. 3, pp. 1941–1951, Mar. 2017.
- [20] J.T. Stauth, M.D. Seeman, and K. Kesarwani, "Resonant switched-capacitor converters for sub-module distributed photovoltaic power management," *IEEE Trans. Power Electron.*, vol. 28, no. 3, pp. 1189–1198, Mar. 2013.
- [21] Z. Qiu and K. Sun, "A photovoltaic generation system based on wide voltage-gain dc-dc converter and differential power processors for dc microgrids," *Chinese J. Electrical Eng.*, vol. 3, no. 1, pp. 84–95, Jun. 2017.
- [22] M. Uno and A. Kukita, "PWM converter integrating switched capacitor converter and series-resonant voltage multiplier as equalizers for photovoltaic modules and series-connected energy storage cells for exploration rovers," *IEEE Trans. Power Electron.*, vol. 32, no. 11, pp. 8500–8513, Nov. 2017.
- [23] P.K. Peter and V. Agarwal, "Current equalization in photovoltaic strings with module integrated ground-isolated switched capacitor dc-dc converters," *IEEE J. Photovoltaics*, vol. 4, no. 2, pp. 669–678, Mar. 2014.
- [24] S.R. Sanders, E. Alon, H.P. Le, M.D. Seeman, M. Jhon, and V.W. Ng, "The road to fully integrated dc-dc conversion via the switched-capacitor approach," *IEEE Trans. Power Electron.*, vol. 28, no. 9, pp. 4146–4155, Sep. 2013.
- [25] M. Uno and A. Kukita, "PWM switched capacitor converter with switched-capacitor-inductor cell for adjustable high step-down voltage conversion," *IEEE Trans. Power Electron.*, vol. 34, no. 1, pp. 425–437, Jan. 2019.
- [26] S. Poshtkouthi, V. Palaniappan, M. Fard, and O. Trescases, "A general approach for quantifying the benefit of distributed powered electronics for fine grained MPPT in photovoltaic applications using 3-D modeling," *IEEE Trans. Power Electron.*, vol. 27, no. 11, pp. 4656–4666, Nov. 2012.

- [27] A.H. Chang, A.T. Avestruz, and S.B. Leeb, "Capacitor-less photovoltaic cell-level power balancing using diffusion charge redistribution," *IEEE Trans. Power Electron.*, vol. 30, no. 2, pp. 537–546, Feb. 2015.
- [28] A.H. Chang and S.B. Leeb, "Differential diffusion charge redistribution for photovoltaic cell-level power balancing," in *Proc. Int. Conf. Renewable Energy Research and Appl. (ICRERA)*, pp. 576–582, 2014.
- [29] M. Uno, Y. Saito, M. Yamamoto, and S. Urabe, "Dual MPPT control and field testing for switched capacitor-based cell-level power balancing utilizing diffusion capacitance of photovoltaic cells," in *Proc. IEEE Int. Power Electron. Conf. (IPEC) 2018, ECCE-Asia*, pp. 1782–1787, May 2018.
- [30] Sunpower. (2010, Nov.) C60 Solar Cell Mono Crystalline Silicon. [Online]. http://eshop.terms.eu/_data/s_3386/files/1379942540-sunpower_c60_bin_ghi.pdf#search=sunpower+C60
- [31] R.A. Kumar, M.S. Suresh, J. Nagaraju, "Measurement and comparison of AC parameters of silicon (BSR and BSFR) and gallium arsenide (GaAs/Ge) solar cells used in space applications," *Solar Energy Material & Solar Cells*, vol. 60, no. 2, pp.397–406, Jan. 2005.
- [32] K.A. Kim, C. Xu, L. Jin, and P.T. Krein, "A dynamic photovoltaic model incorporating capacitive and reverse-bias characteristics," *IEEE J. Photovoltaics*, vol. 3, no. 4, pp. 1334–1341, Oct. 2013.
- [33] C.R. Jeevandoss, M. Kumaravel, and V.J. Kumar, "A novel measurement method to determine the C–V characteristic of a solar photovoltaic cell," *IEEE Trans. Instrumentation Measurement.*, vol. 60, no. 5, pp. 176–1767, May 2011.
- [34] Semiconductor Equipment and Materials International (SEMI) Standards Program, Contactless Carrier-Lifetime Measurement in Silicon Wafers, Ingots, and Blocks, AUX017-0310E, 2010.
- [35] K.A. Kim, P.S. Shenoy, and P.T. Krein, "Converter rating analysis for photovoltaic differential power processing systems," *IEEE Trans. Ind. Electron.*, vol. 30, no. 4, pp. 1987–1997, Apr. 2015.
- [36] C.H. Kim, M.Y. Kim, and G.W. Moon, "A modularized charge equalizer using a battery monitoring IC for series-connected Li-ion battery strings in electric vehicles," *IEEE Trans. Power Electron.*, vol. 28, no. 8, pp. 3779–3787, Aug. 2013.
- [37] Z. Zhang, H. Gui, D.J. Gu, Y. Yang, and X. Ren, "A hierarchical active balancing architecture for lithium-ion batteries," *IEEE Trans. Power Electron.*, vol. 32, no. 4, pp. 2757–2768, Apr. 2017.
- [38] B. Dong, Y. Li, and Y. Han, "Parallel architecture for battery charge equalization," *IEEE Trans. Power Electron.*, vol. 30, no. 9, pp. 4906–4913, Sep. 2015.
- [39] M.D. Seeman and S.R. Sanders, "Analysis and optimization of switched-capacitor dc-dc converters," *IEEE Trans. Power Electron.*, vol. 23, no. 2, pp. 841–851, Mar. 2008.
- [40] B. Oraw and R. Ayyanar, "Load adaptive, high efficiency, switched capacitor intermediate bus converter," in *Proc. IEEE Int. Telecommun. Energy Conf., INTELEC'07*, pp. 1872–1877, 2007.
- [41] M. Uno, "Unregulated interface converter based on cascaded switched capacitor converters for super-capacitors in alternative battery applications," in *Proc. IEEE Power Electron. Drive Systems*, pp. 579–586, Dec. 2011.
- [42] G.V. Piqué, H.J. Bergveld, and E. Alarcón, "Survey and benchmark of fully integrated switching power converters: switched-capacitor versus inductive approach," *IEEE Trans. Power Electron.*, vol. 28, no. 9, pp. 4156–4167, Sep. 2013.



Yota Saito was born in Japan in 1994. He received the B.E. degree in electrical engineering from Ibaraki University, Hitachi, Japan, in 2017, where he is currently working toward the M.E. degree in electrical engineering at the Graduate School of Science and Engineering. His research interests include switching converters for photovoltaic systems.



Shinichi Urabe was born in Japan in 1975. He received the M.S. degree in Precision Science from Osaka University, in 2000, and his major was semiconductor material. From 2000 to 2007, he worked for Omron Corporation and developed sensing technologies for factory automation systems. Since 2007, he has been with Toyota Motor Corporation, where he is currently studying differential power processing converters.



Masaya Yamamoto was born in Japan in 1992. He received the B.E. degree and M.E degree in electrical engineering from Ibaraki University, Ibaraki, Japan, in 2016 and 2018, respectively. Since 2018, he has been with SEIKO EPSON corporation. His research interests include switching converters for photovoltaic systems.



Masatoshi Uno (M'06) was born in Japan in 1979. He received the B.E. degree in electronics engineering and the M.E. degree in electrical engineering from Doshisha University, Kyoto, Japan, and the Ph.D. degree in space and astronomical science from the Graduate University for Advanced Studies, Hayama, Japan, in 2002, 2004, and 2012, respectively.

In 2004, he joined the Japan Aerospace Exploration Agency, Sagami-hara, Japan, where he developed spacecraft power systems including battery, photovoltaic, and fuel cell systems. In 2014, he joined the Department of Electrical and Electronics Engineering, Ibaraki University, Ibaraki, Japan, where he is currently an Associate Professor of Electrical Engineering.

His research interests include switching power converters for renewable energy systems, life evaluation for EDLCs and lithium-ion batteries, and development of spacecraft power systems. Dr. Uno received the Isao Takahashi Power Electronics Award in 2018.